6 Chapter 6

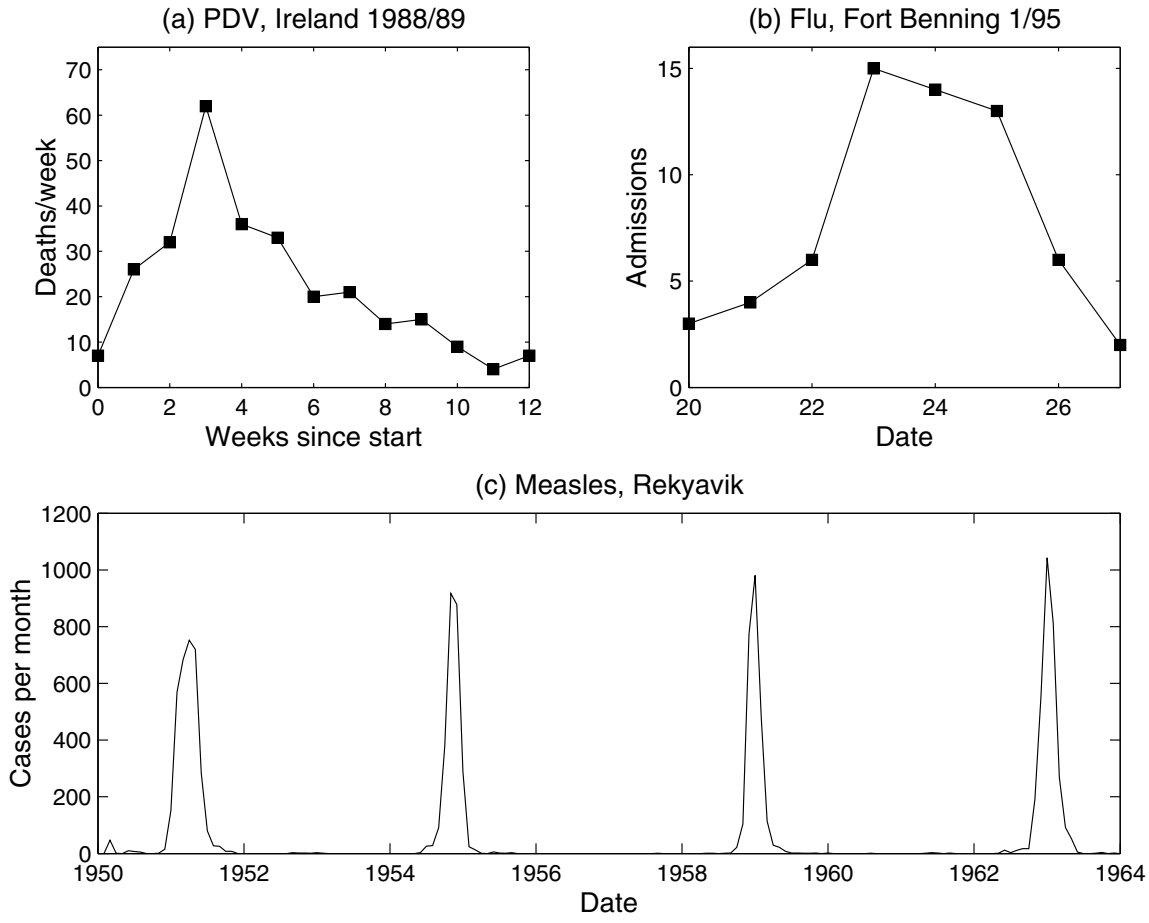

Figure 6.1: Examples of epidemic curves. (a) Phocine distemper virus in Northern Ireland 1988/89 (data from Figure 4 of Hall et al. 1992, provided by John Harwood). (b) An outbreak of influenza in Fort Benning, Georgia in 1995 (data from Davidson 1995). (c) Recurrent outbreaks of measles in Rekyavik, Iceland (data provided by Andrew Cliff, Department of Geography, University of Cambridge).

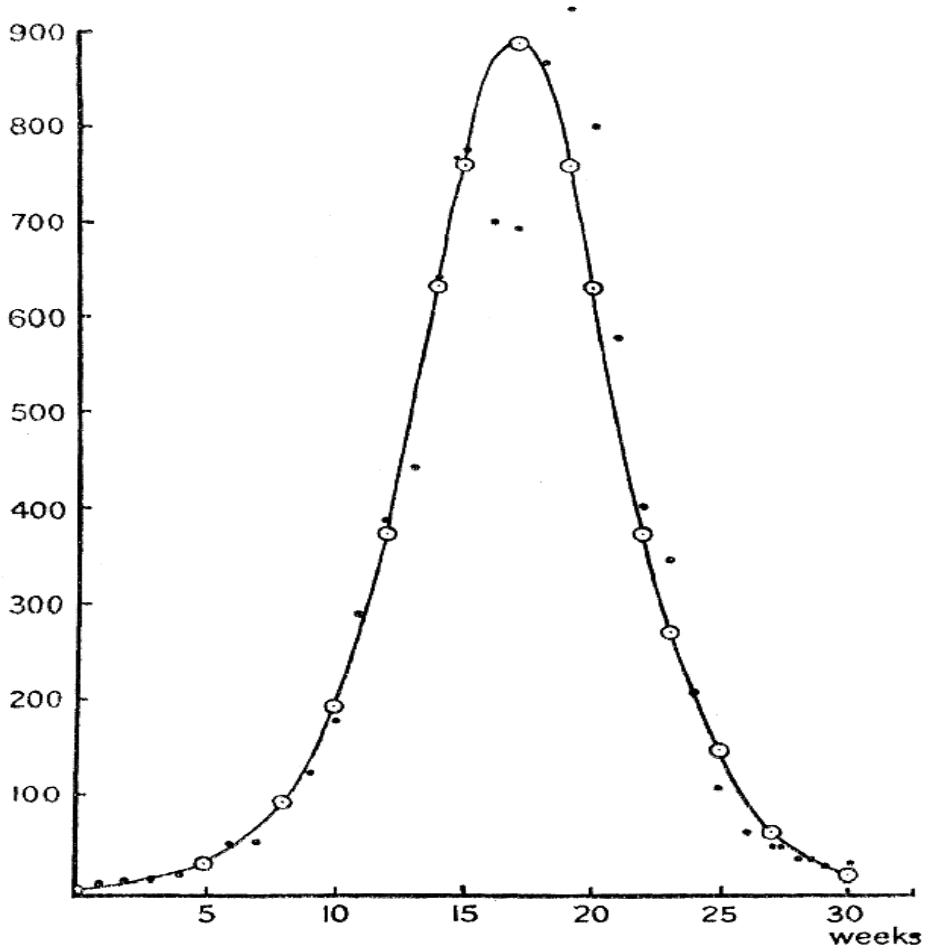

Figure 6.2: Deaths per week from plague in the island of Bombay from December 17, 1905 to July 21, 1906, from Kermack and McKendrick (1927). The solid line is an approximate solution to their model for a disease with permanent removal – death or immunity – in the rat population on the island. It is compared with data on the human death toll on the assumption that "plague in man is a reflection of plague in rats."

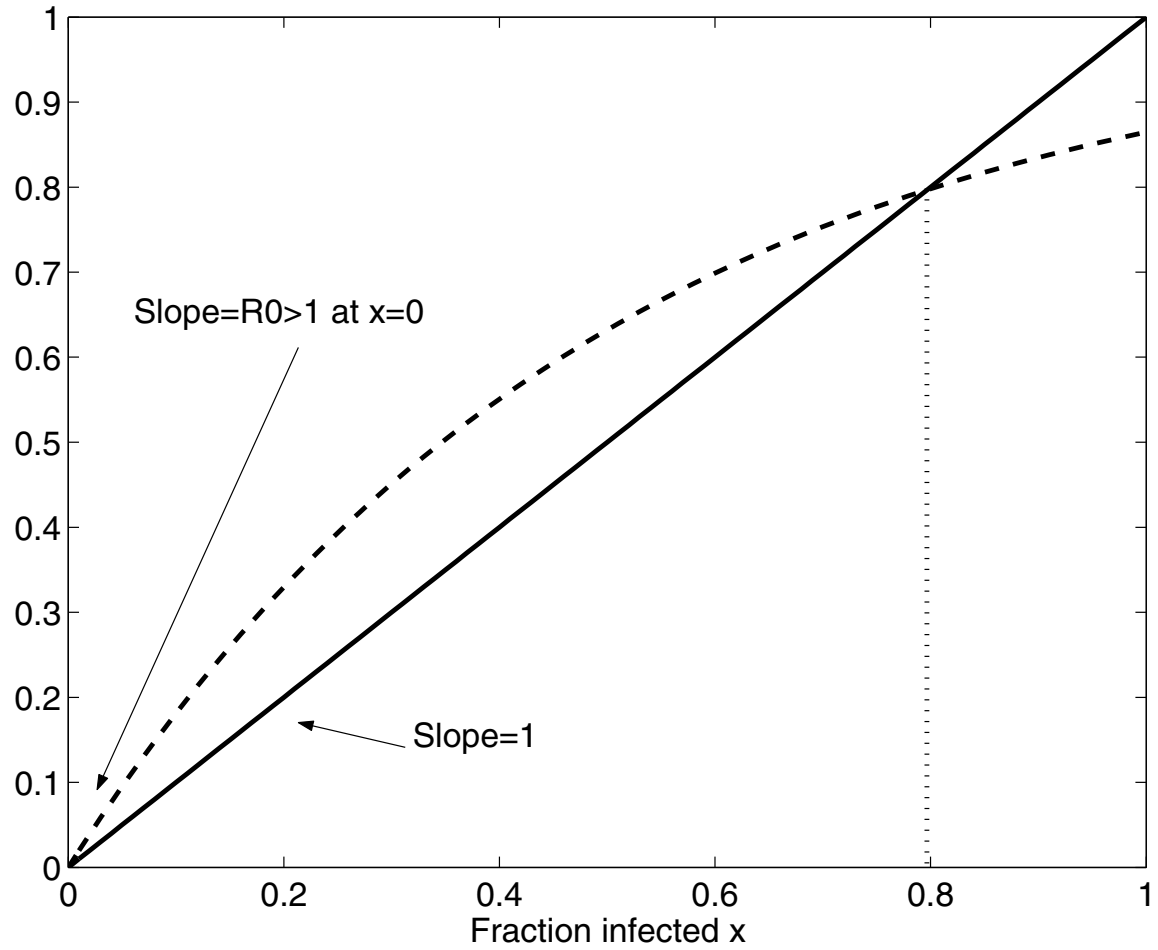

Figure 6.3: Graphical illustration that the final size equation has a unique solution between $x = 0$ and $x = 1$. The solution gives the approximate fraction of the population that contracted the disease over the course of an epidemic (Z_∞) in the Kermack-McKendrick SIR model, when the epidemic starts with a small number of infectives and the rest of the population susceptible.

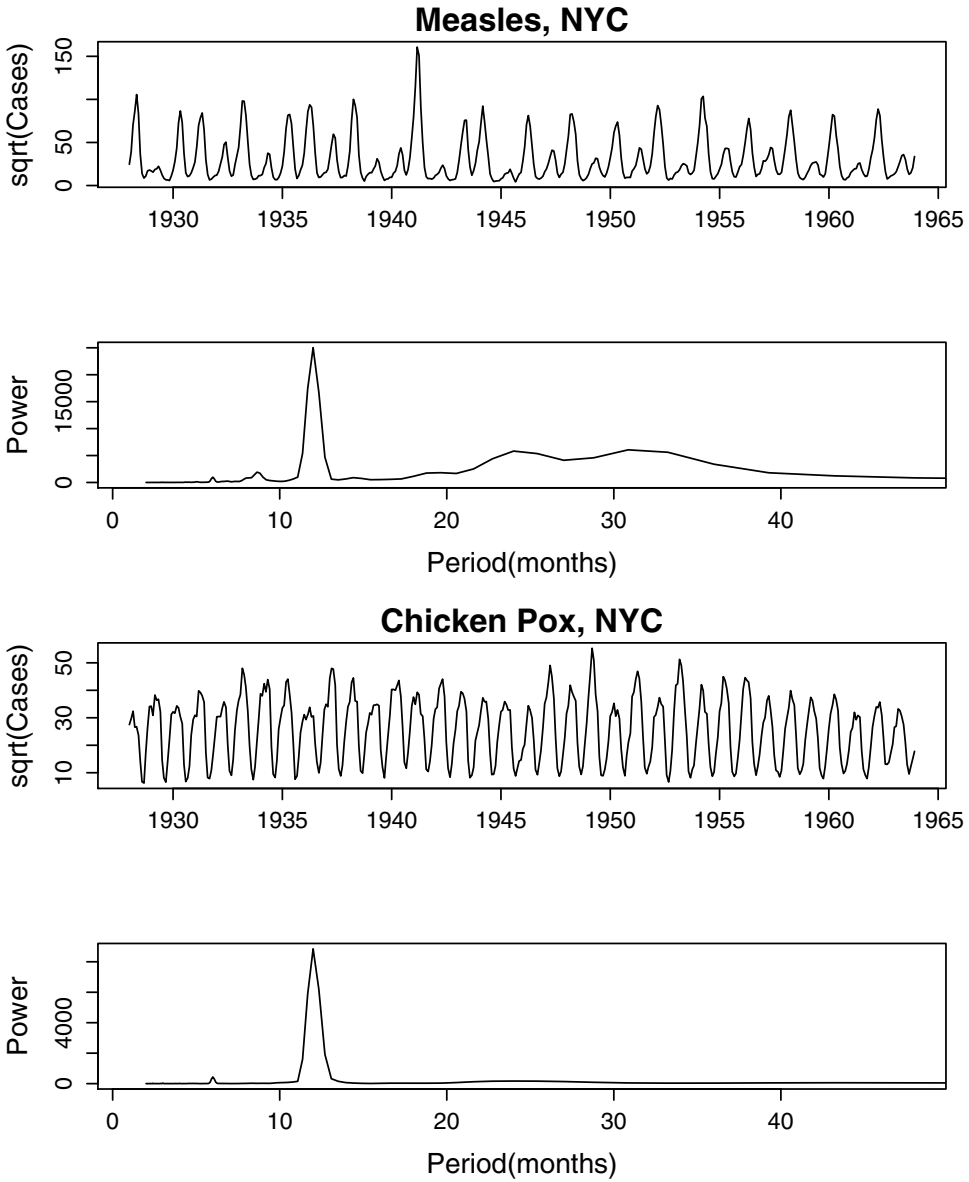

Figure 6.4: Monthly case report totals for measles and chickenpox in New York City prior to vaccination, plotted on square-root scale, and power spectra of the case report time series. The *power spectrum* of a time series represents the relative importance of different oscillation frequencies in the data. The spectra shown here confirm that chickenpox is dominated by a simple annual cycle, while measles shows a mix of annual, two-year, and three-year cycles.

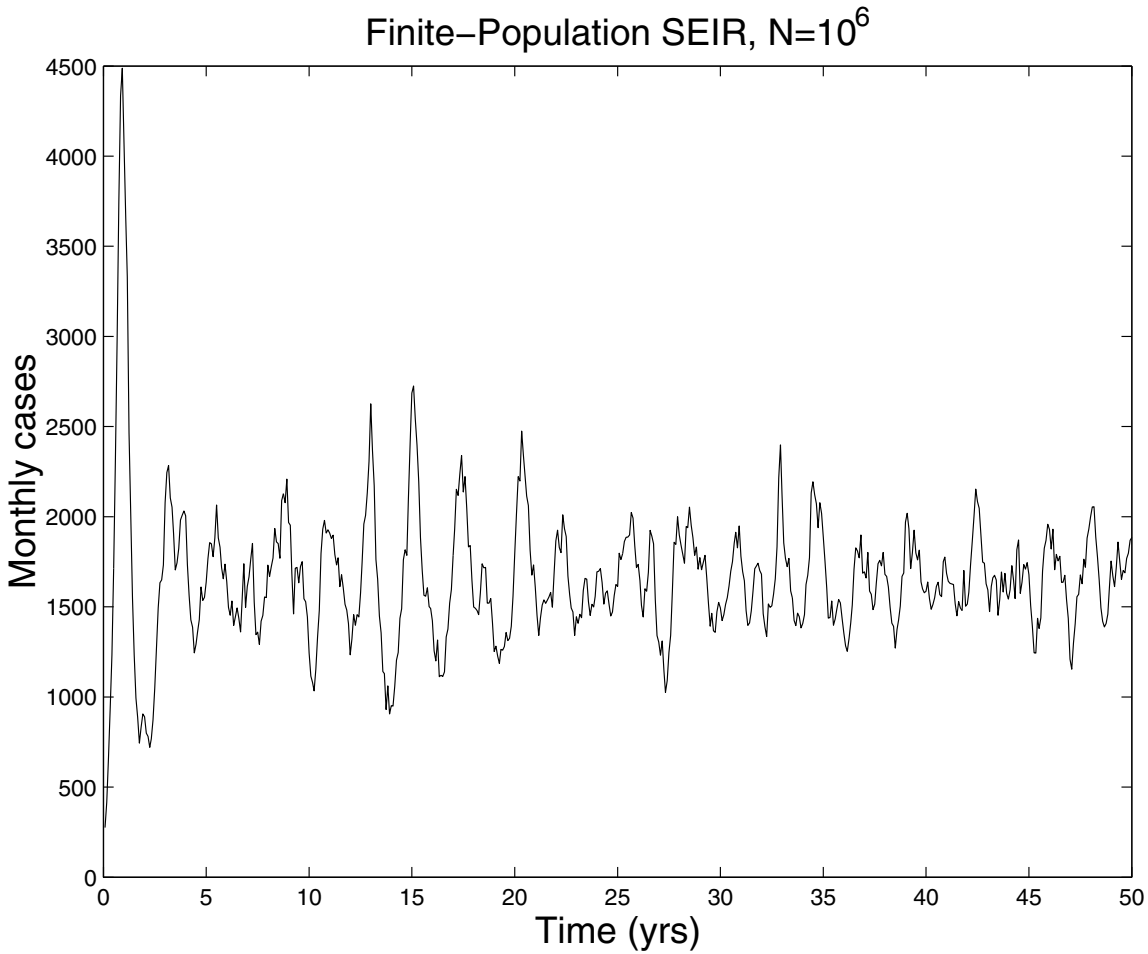

Figure 6.5: Output from a finite-population SEIR model with parameters appropriate for pre-vaccination dynamics of measles in a city of 1 million, but without any seasonal variation in the transmission rate.

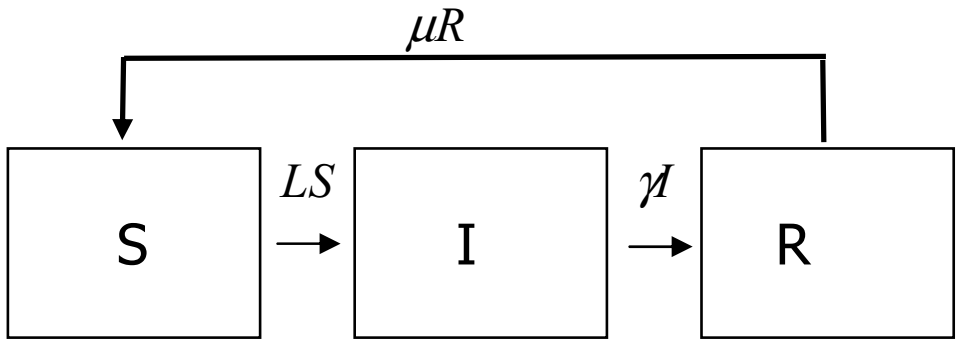

Figure 6.6: Compartment diagram for discrete-event SIR model.

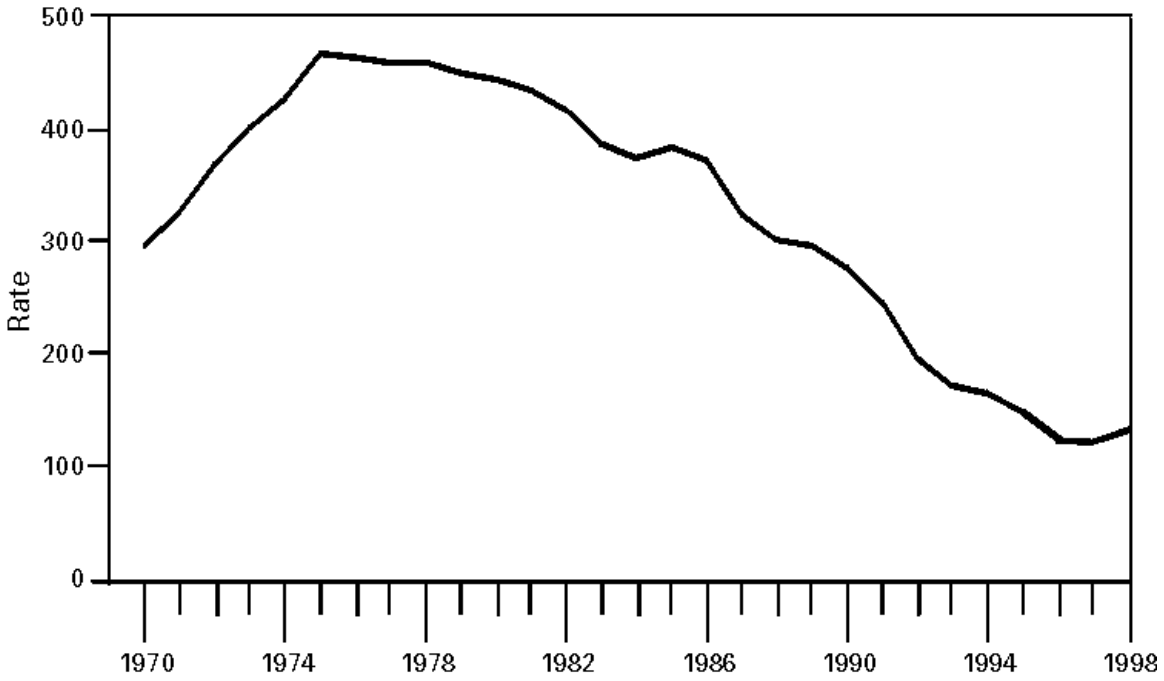

Figure 6.7: Reported gonorrhea rate (cases per 100,000 population) in the United States, from CDC 2000

.

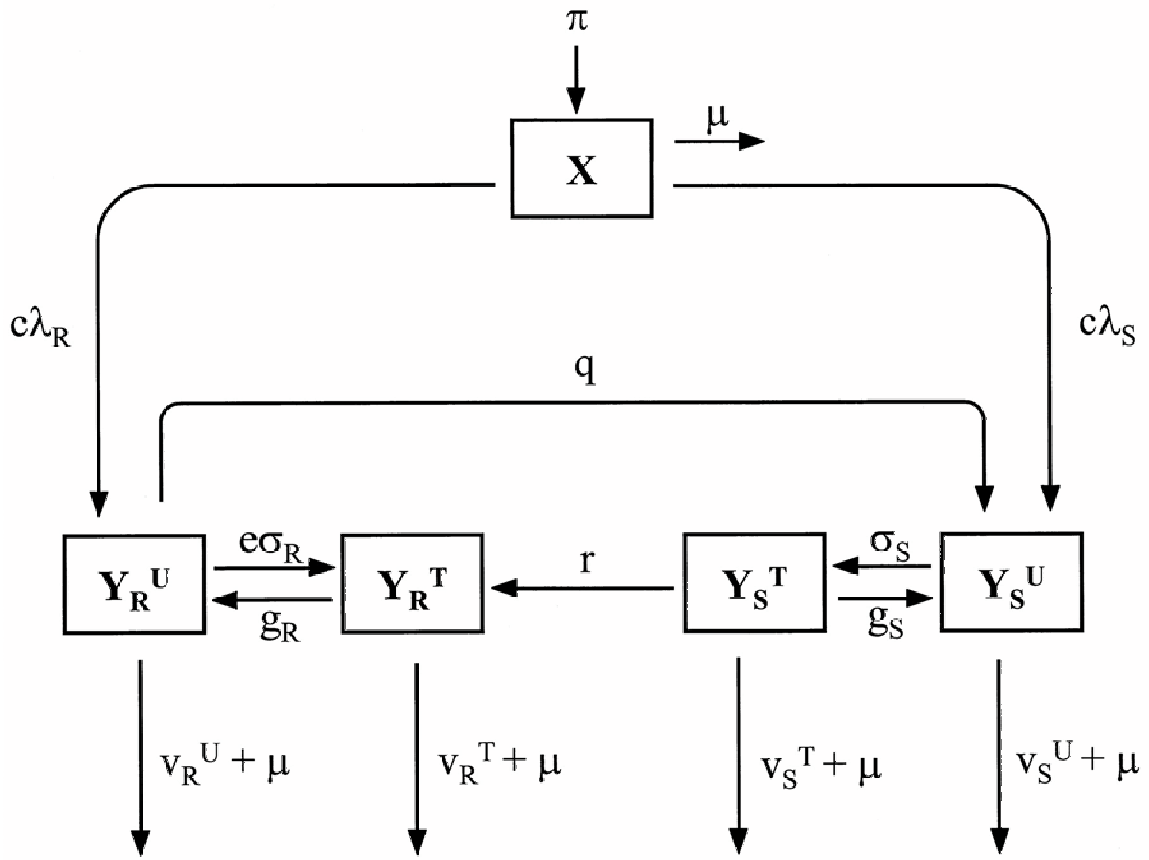

Figure 6.8: Compartment diagram from Blower et al. (2000) for their model for HIV transmission dynamics in the presence of antiretrovivral therapy, with both resistant and non-resistant strains circulating in the population.

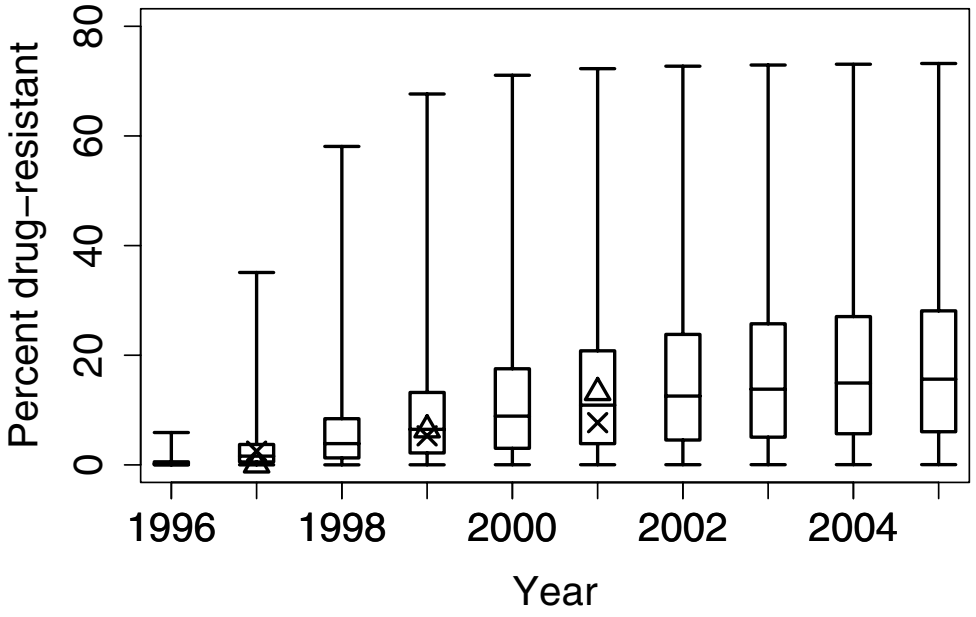

Figure 6.9: Fraction of new HIV infections that are resistant to combination ARV treatment: theoretical predictions versus empirical data for San Francisco (redrawn from Blower et al. 2003 using data provided by S. Blower). Model simulations were run over the time period 1996-2005, with initial conditions corresponding to estimated values for 1996. Boxes enclose the interquartile range (25^{th} to 75^{th} percentiles) of model outcomes and bars show outlier cutoffs; the bars inside the boxes are the median values. Triangles show resistance to non-nucleoside reverse transcriptase inhibitor, and crosses show resistance to protease inhibitor, in a study of 243 newly infected individuals in San Francisco from 1996 to 2001 who had no previous exposure to ARV drugs.

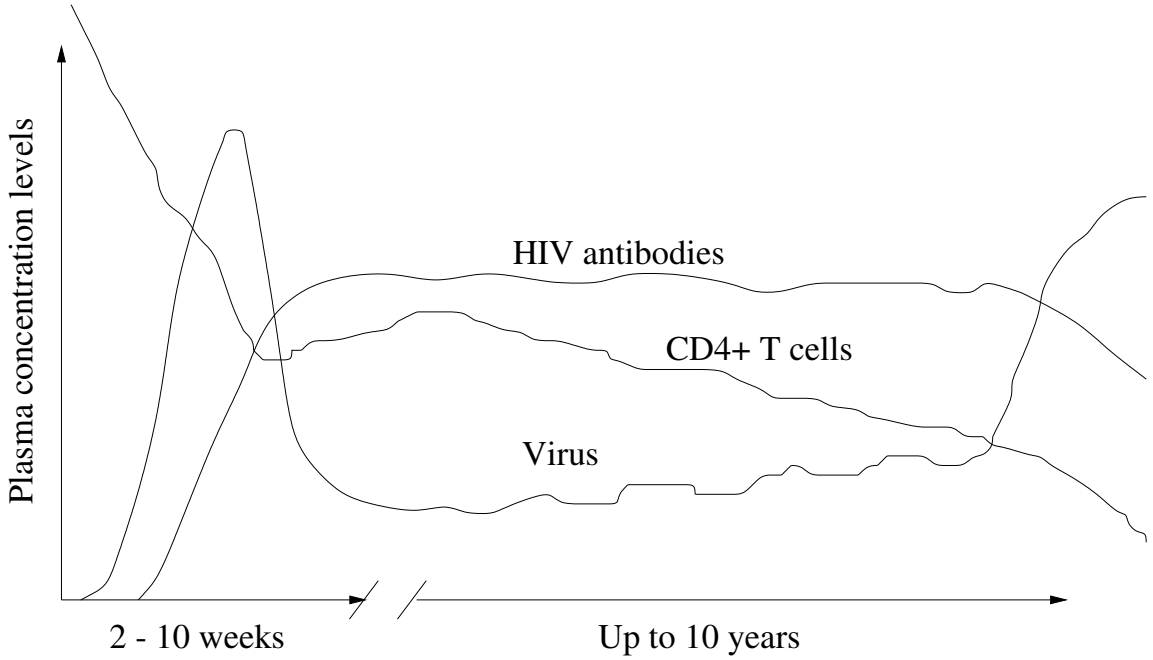

Figure 6.10: Schematic depiction of the typical course of HIV infection in an adult. The early peak in viral load corresponds to the primary infection or "acute" phase. Also shown are T-cell dynamics. From Perelson and Nelson (1999).

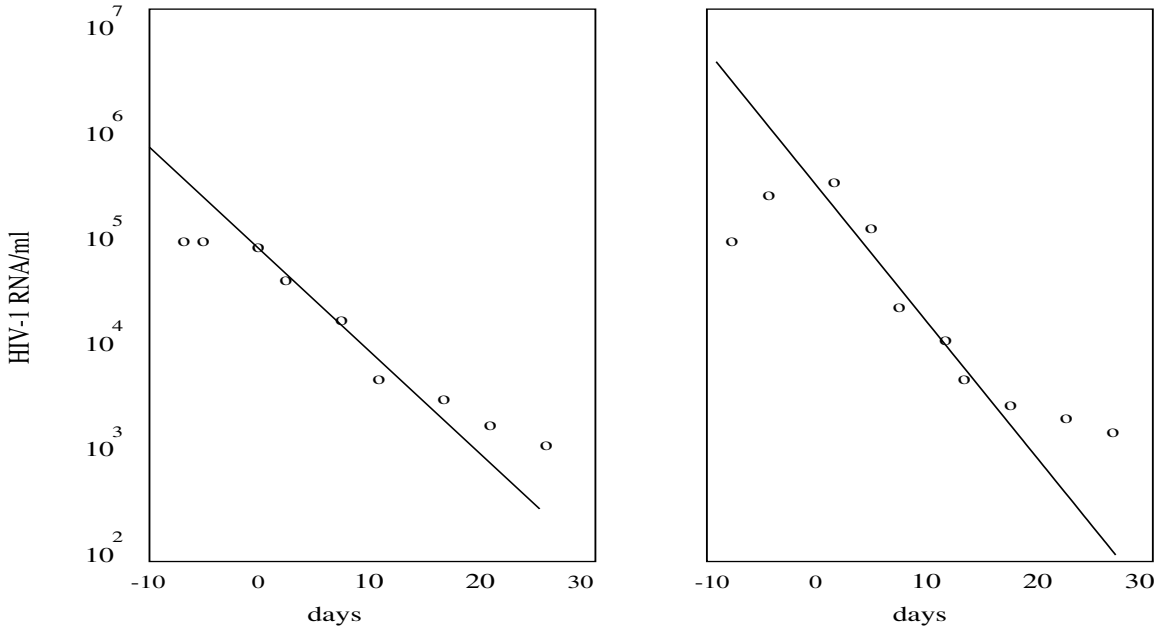

Figure 6.11: Decay of plasma viral load in two patients following treatment with a protease inhibitor. Treatment is initiated at $t = 0$. From Perelson and Nelson (1999), using data from Ho et al. (1995).

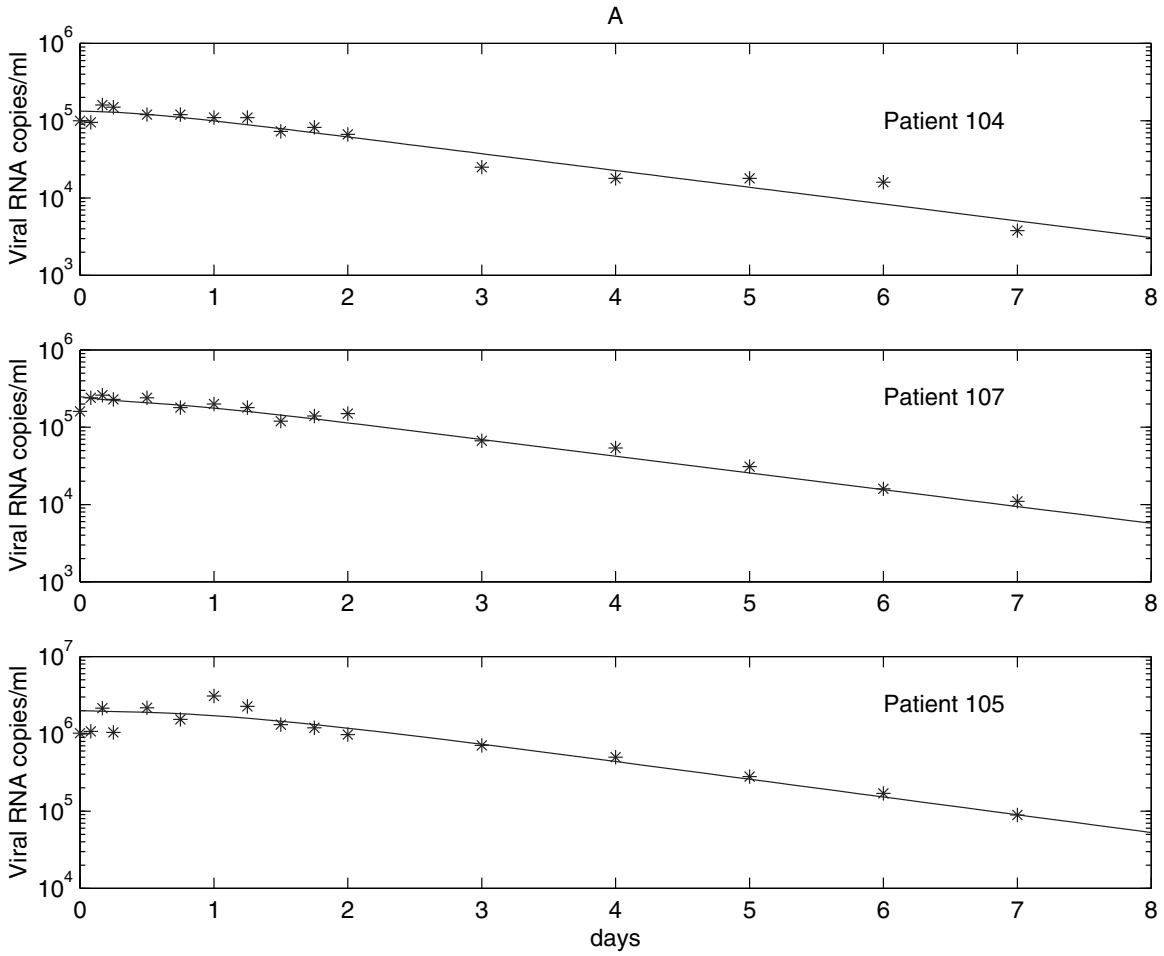

Figure 6.12: Viral load data (symbols) versus model predictions (solid line) during first phase of viral decay after onset of treatment ($t = 0$). From Perelson and Nelson 1999, after Perelson et al. 1996.

7 Chapter 7

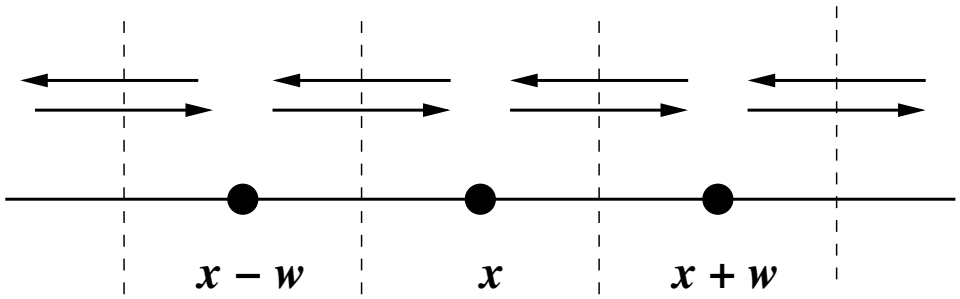

Figure 7.1: Depiction of particles undergoing a random walk on the line with general step-size w.

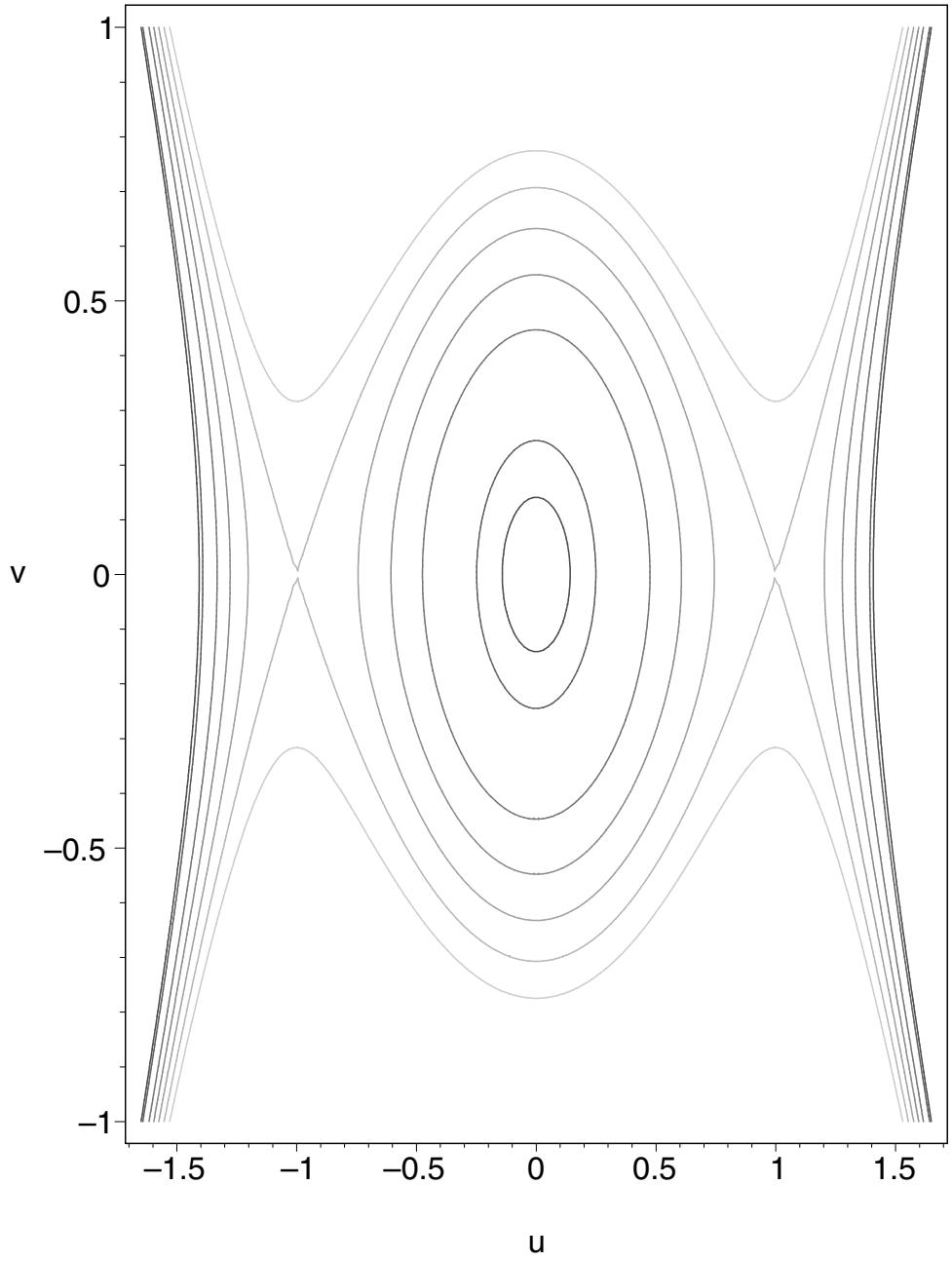

Figure 7.4: Level curves of the function $E(u,v) = \frac{1}{2}v^2 + \frac{a}{2D}u^2 - \frac{1}{4D}u^4$.

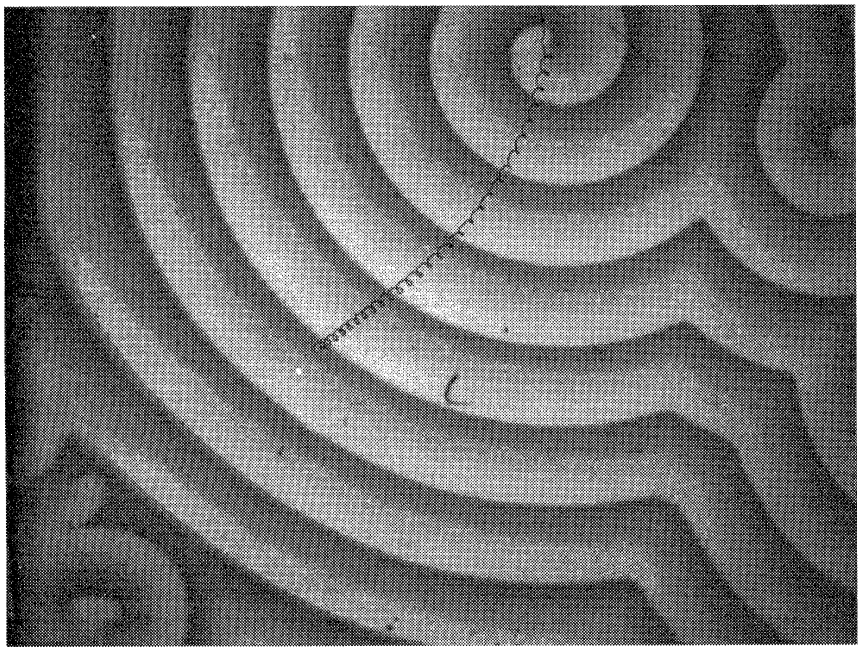

Figure 7.5: Spiral patterns of the BZ reaction, from Winfree et. al. (1996).

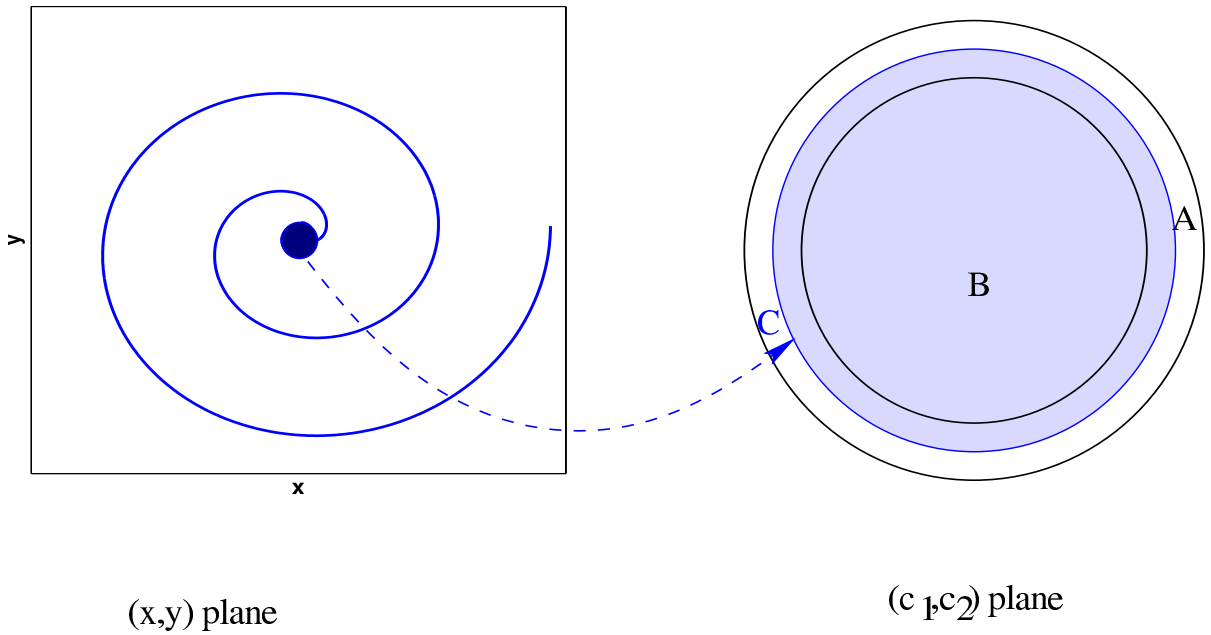

Figure 7.6: Map of spiral wave in the (x, y) plane into the (c_1, c_2) concentration plane. The dark core of the spiral in the (x, y) plane is mapped into the shaded region in the (c_1, c_2) plane, stretching over the disk B. The boundary of the core is mapped onto the curve C bounding the shaded region, making one turn around B. All of the points outside the core are mapped into the annulus A.

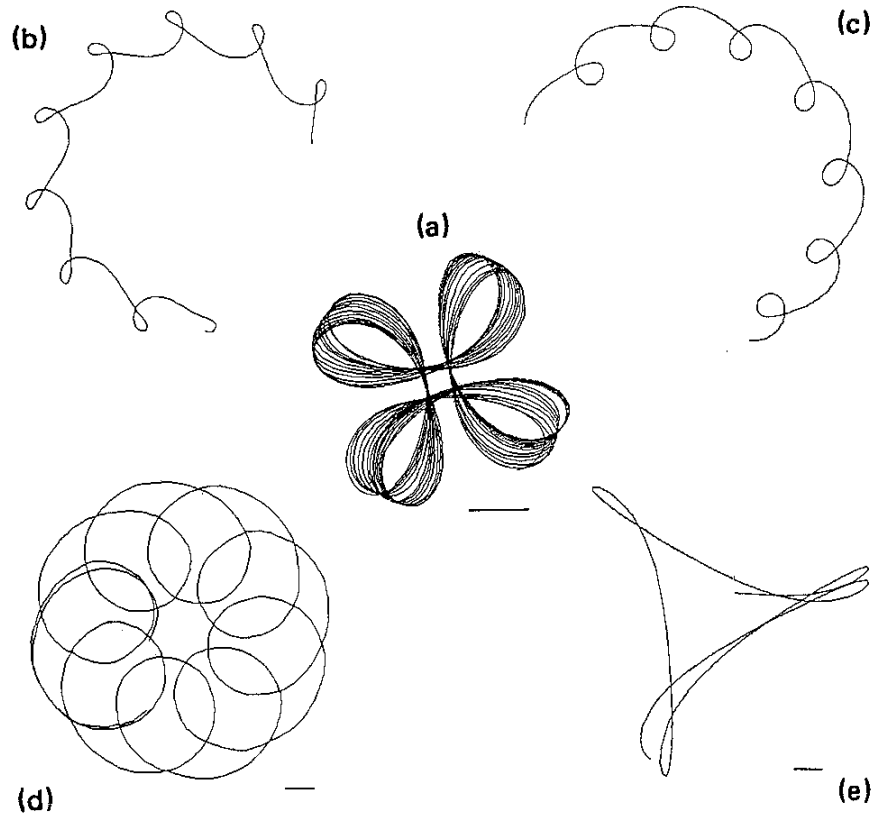

Figure 7.7: (Meandering paths of spiral cores in simulations of a reaction-diffusion system (from Winfree (1991)).

8 Chapter 8

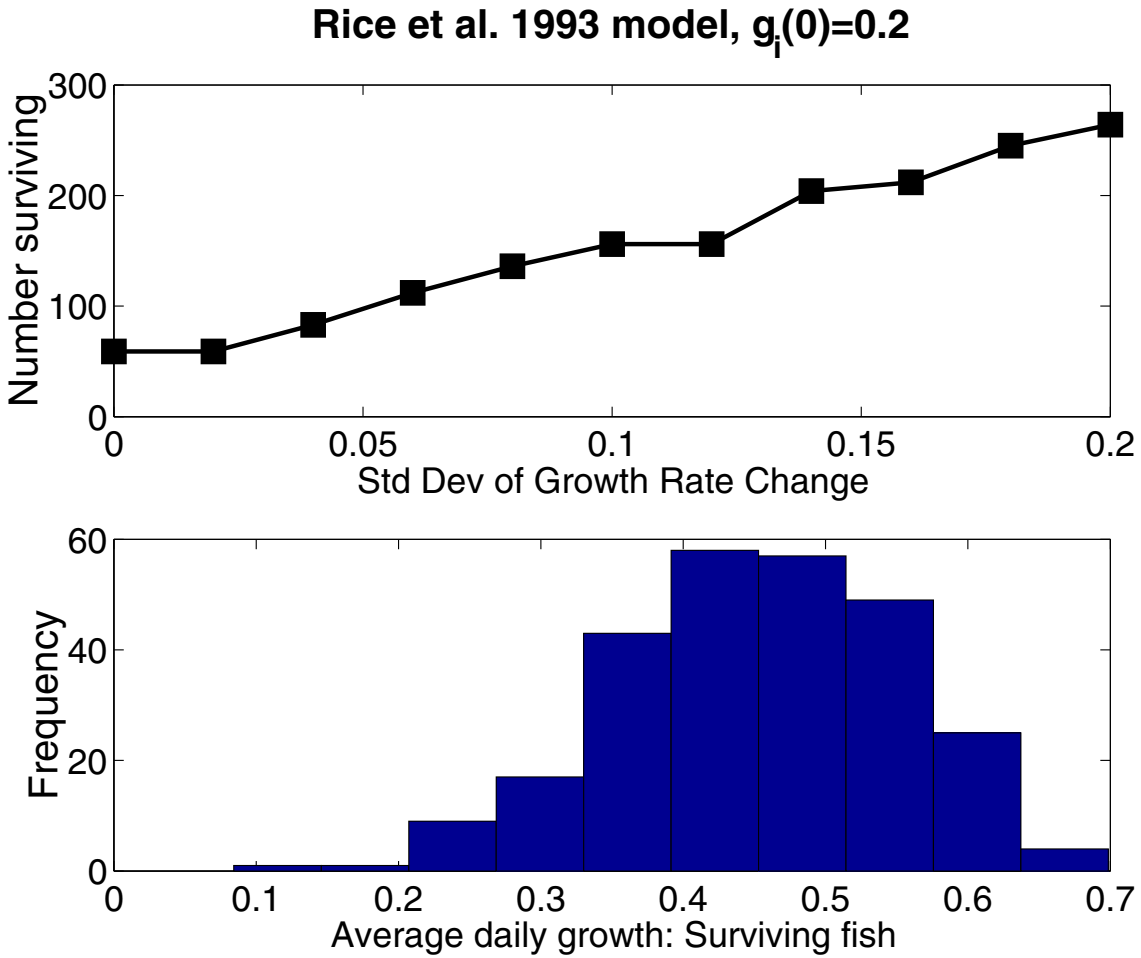

Figure 8.1: Results from simulations of the Rice et al. (1993) individual based model for larval fish growth and survival in the presence of size-dependent predation. Individuals were started at $12mm$ with $g_i(0) = 0.2mm/d$, and were constrained to have growth rate between 0 and $0.8mm/d$, as in Rice et al. (1993).

```
nfish=5000; ndays=50; %5000 fish for 50 days
sizes=zeros(ndays,nfish); growth=zeros(ndays,nfish);
alive=ones(1,nfish);
sigmag=0.08; % standard deviation of changes in growth

% initial sizes and growth rates
sizes(1,1:nfish)=0.4*ones(1,nfish);
growth(1,1:nfish)=0.4;

%iterate the model
for jday=1:(ndays-1);
    % Predation. For simplicity of coding, the dead can die again.
    meetpred=rand(1,nfish)<0.2; %does a predator find me?
    pdie=-0.33 + 0.15*(90./sizes(jday,:)); %if so....
    eaten=rand(1,nfish)<pdie;
    m=find(meetpred.*eaten>0);   % do I live or die?
    alive(m)=0;
    % find sizes and growth rates for tomorrow
    sizes(jday+1,:)=sizes(jday,:)+growth(jday,:);
    growth(jday+1,:)=growth(jday,:)+sigmag*randn(1,nfish);
    growth(find(growth<0))=0;
    growth(find(growth>0.8))=0.8;
end;

% plot growth rate of survivors
m=find(alive>0); growthrate=(sizes(ndays,m)-sizes(1,m))/ndays;
hist(growthrate);
```

Table 1: MATLAB code for the Rice et al. (1993) model with random changes in growth rate over time.

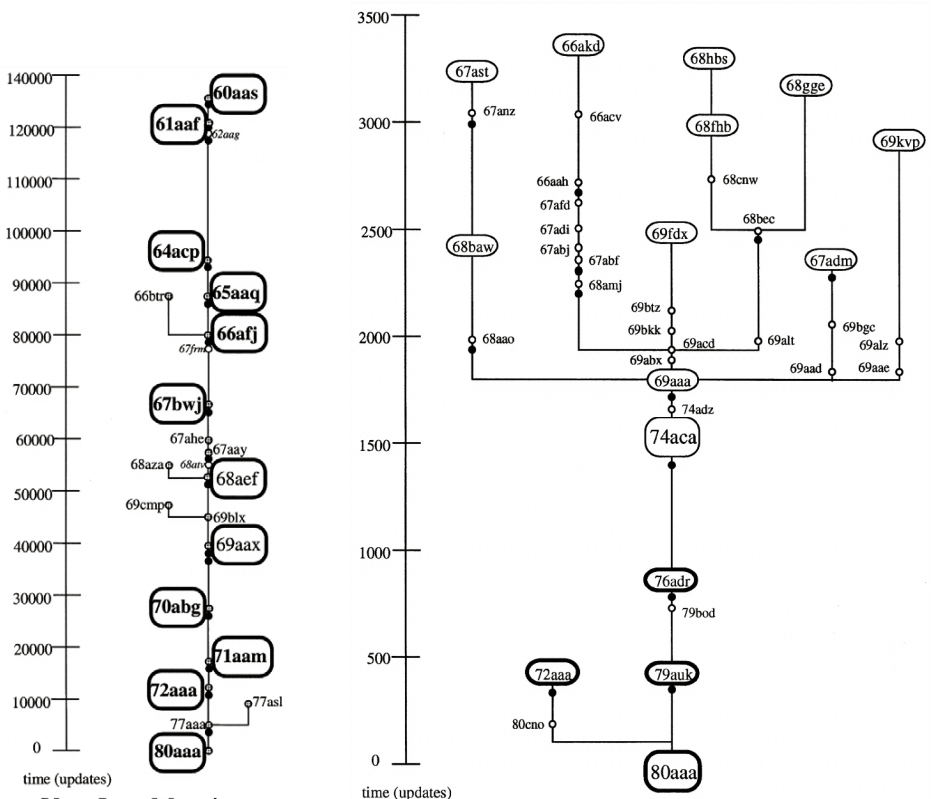

Very Low Mutation

High mutation

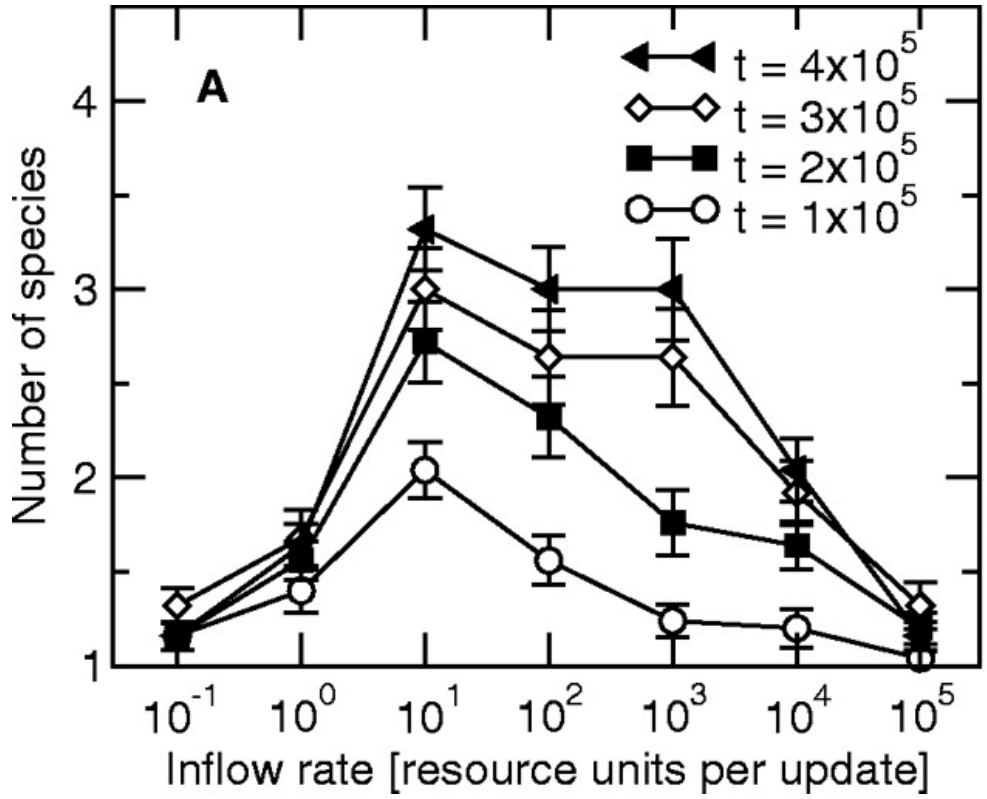

Figure 8.3: Relationship between resource supply rate and the number of distinct species descended from the ancestor, at different times in the simulation (time t is measured in "updates", corresponding roughly to the CPU time required for 30 instructions to be executed).

Parameter	Optimistic			Pessimistic		
	Year 1	Year 5	Year 10	Year 1	Year 5	Year 10
Fraction of drug-sensitive cases treated	0.99	0.99	0.99	0.97	0.97	0.95
Transmission coefficient of drug-sensitive treated infection	-0.18	-0.65	-0.84	-0.10	-0.43	-0.60
Average survival time of drug-sensitive treated individuals	0.86	0.85	0.78	0.52	0.35	0.26
Increase in risky behavior				-0.86	-0.89	-0.90

Table 2: Sensitivity coefficients for key parameters in the Blower et al. (2000) model for antiretroviral treatment of HIV/AIDS, taken from Table 1 of that paper. The model output variable was the number of AIDS deaths averted by treatment, and the tabulated values are partial rank correlation coefficients between parameters and output where the correlation was above 0.5 in magnitude. "Optimistic" and "pessimistic" scenarios differ in their assumptions about the fraction of treated infections where resistance develops and the possible rate at which risky behaviors increase.

Parameter group	M_i	T_i
Parr per spawner	0.38	0.39
Parr to smolt survival	0.01	0.09
Smolt to adult survival	0.52	0.54
Proportional spawning at age 4	0.01	0.001

Table 3: Main and total Sobol' sensitivity indices for stage-specific parameter groups in a stochastic age-structured model for salmon populations, using parameter input distributions corresponding to the uncertainty in parameter estimates (Ellner and Fieberg 2003). The response variable Y is the predicted long term population growth rate, estimated from 5000 model runs at each parameter set. The exact values of the indices must satisfy $M_i < T_i$, but this may not hold for estimated values that are computed from a finite sample of parameters. From Ellner and Fieberg (2003)

.

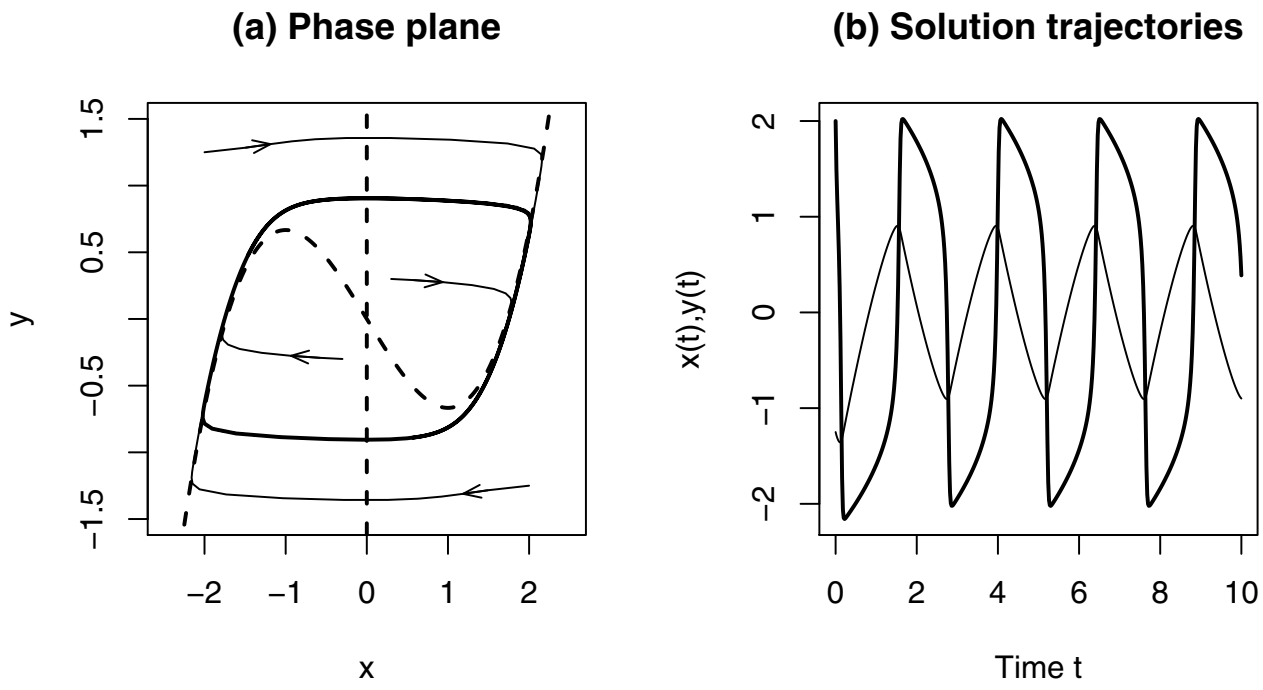

Figure 8.4: Relaxation oscillations in the VanDerPol model with $C = 20$. In the phase portrait (a) the nullclines are drawn as dashed lines, and four solution trajectories as solid lines. All trajectories converge very quickly onto the limit cycle, drawn in bold. Panel (b) shows the state variables $x(t)$ (bold) and $y(t)$.

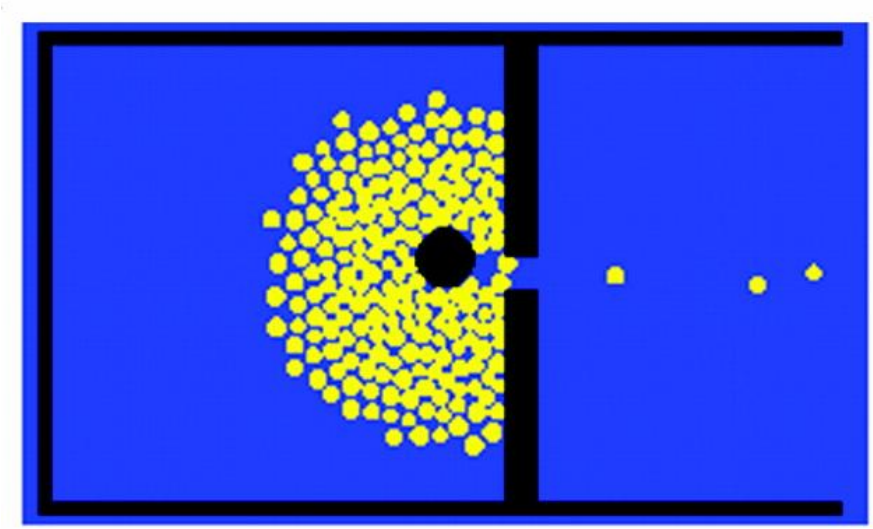

Figure 8.5: A simulation of the Helbing et al. (2000) model for exit panic with a column placed asymmetrically in front of the exit, from Bonabeau (2002). The presence of the column causes the agents to organize their movements in a way that decreases the number of injuries and increases the rate of exit.

9 Chapter 9

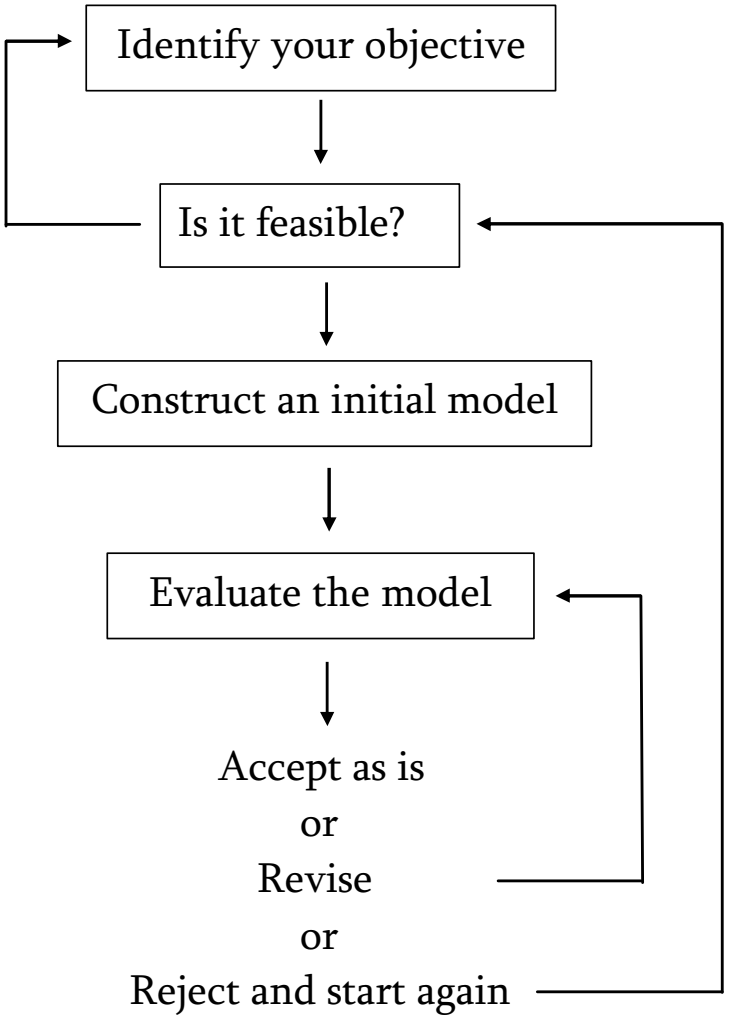
Identify your objective
Is it feasible?
Construct an initial model
Evaluate the model
Accept as is
or
Revise
or
Reject and start again

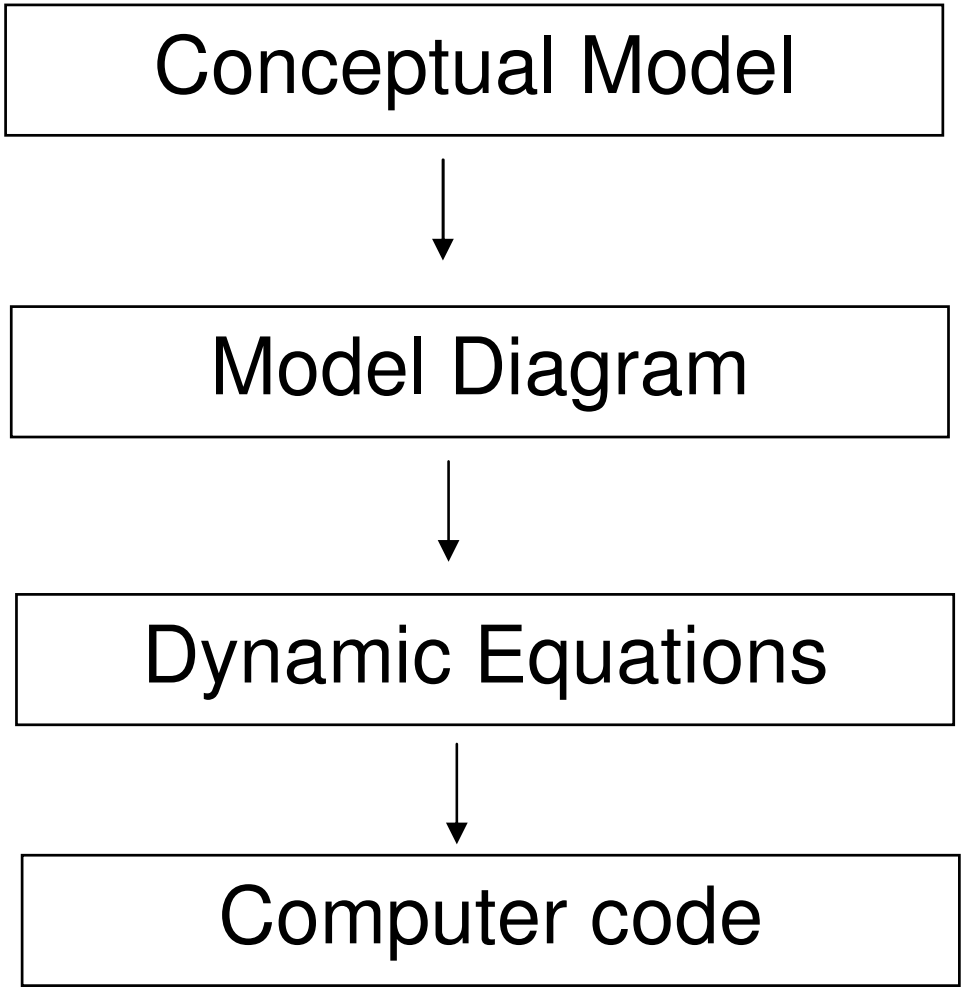

Figure 9.2: Outline of the steps in developing a model.

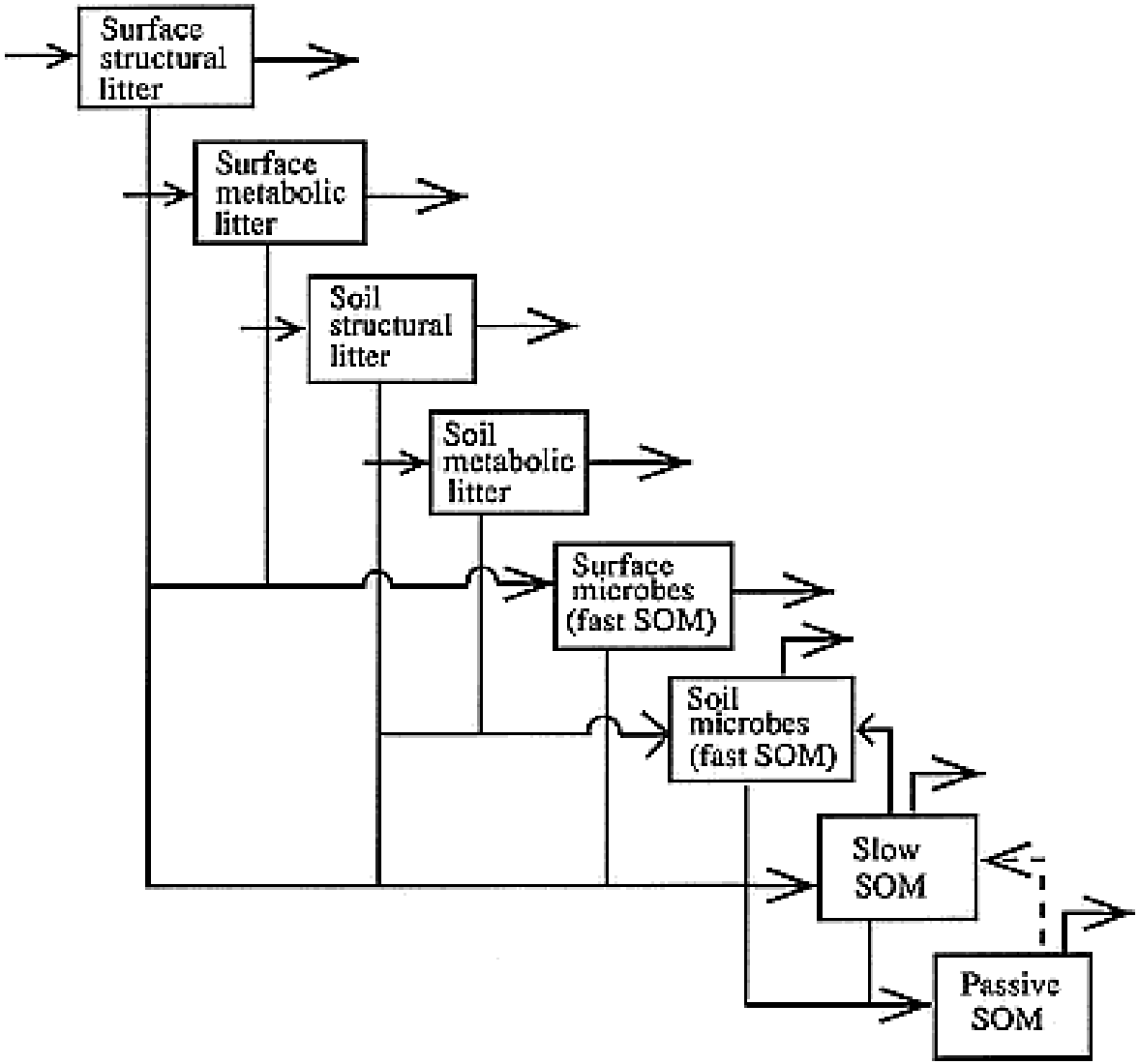

Figure 9.3: Diagram of the compartments for soil organic matter in the CENTURY model, from Bolker et al. 1998. The dotted arrow (from the passive to the slow pool of decomposing organic matter in the soil) represents a very small flow.

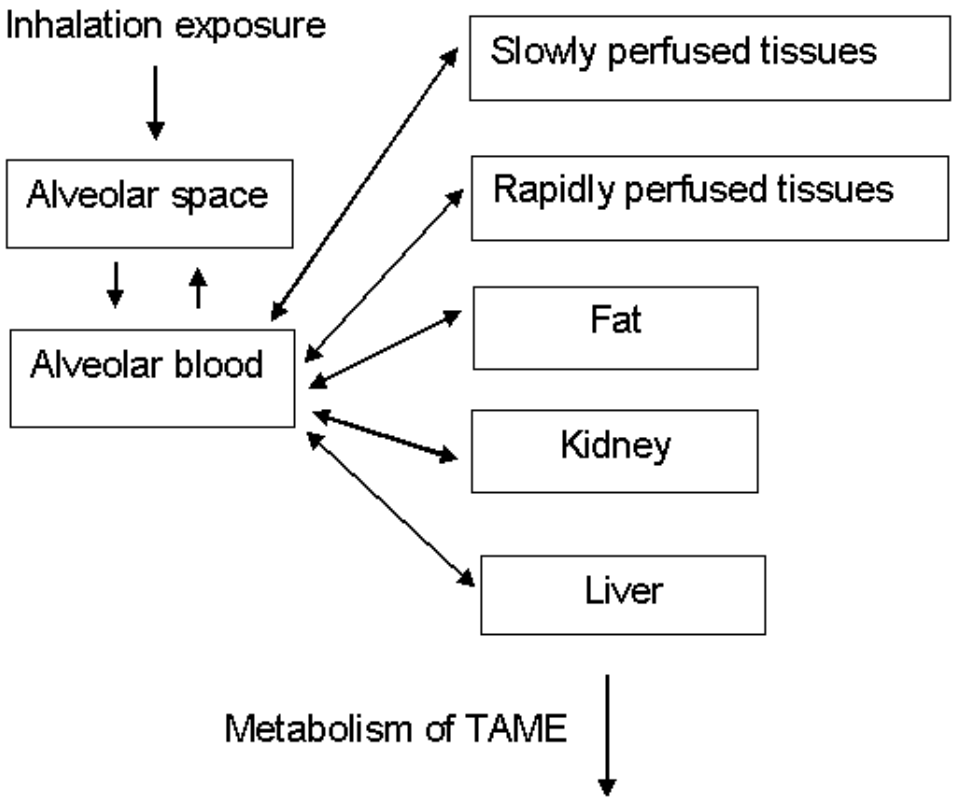

Figure 9.4: Compartment diagram of the model for TAME in the rat proposed by Collins et al. 1999. Double-headed arrows indicate a pair of flows, one in each direction, between two compartments.

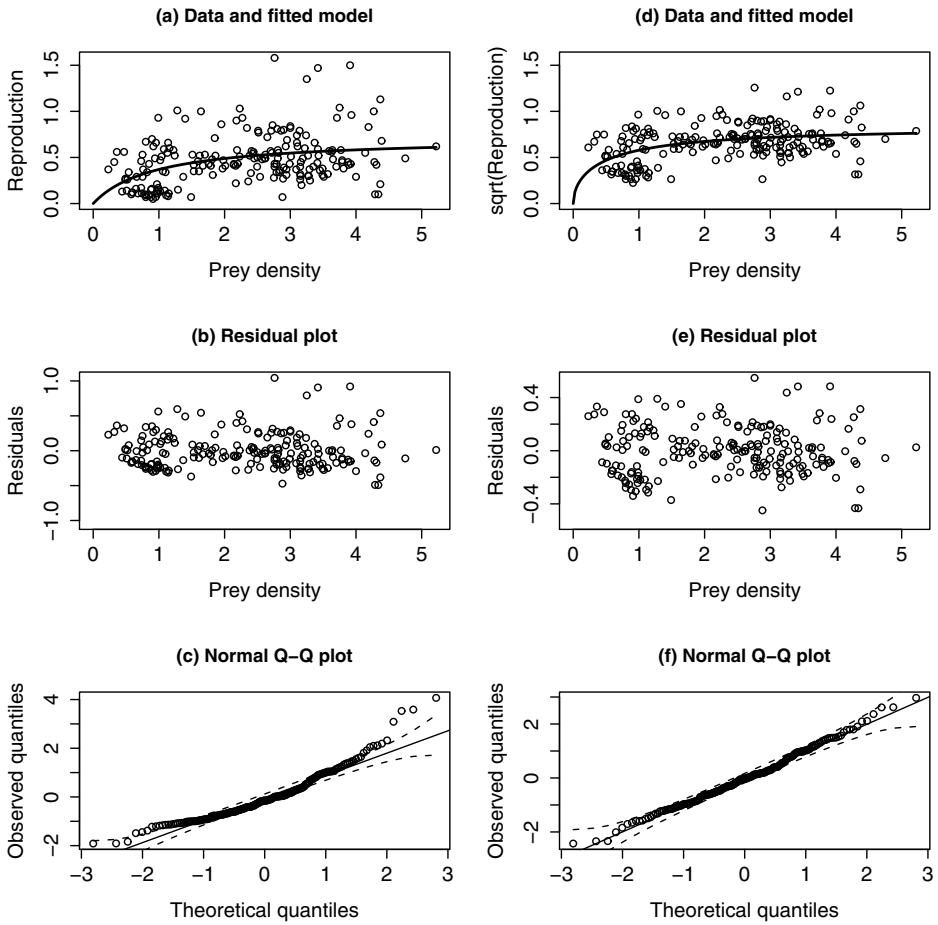

Figure 9.5: Fitting a parametric rate equation model. (a) The data and fitted curve (b) Residuals plotted against the independent variable (c) Quantile-quantile plot comparing the distribution of residuals to the Gaussian distribution assumed by the least-squares fitting criterion (d) Data and fitted curve on square root scale (e) Residuals from model fitted on square root scale (f) Quantile-quantile plot for square root scale residuals. The dashed curves in panels (c) and (f) are pointwise 95% confidence bands; the large number of points outside the confidence bands in panel (c) show that the residuals do not conform to a Gaussian distribution.

1. Concave up, increasing

$y = ax^b \qquad a > 0, b > 1$

$y = ae^{bx} \qquad a > 0, b > 0$

$y = a + bx + cx^2 \qquad c > 0$

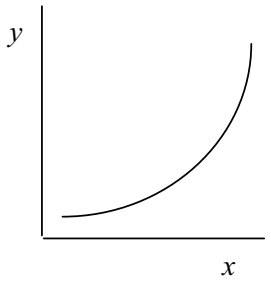

2. Concave down, increasing

$y = ax^b \qquad a > 0, b < 1$

$y = ax/(b + x) \qquad a > 0, b > 0$

$y = a + bx + cx^2 \qquad b > 0, c < 0$

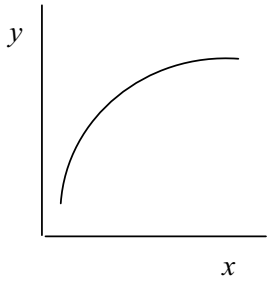

3. Concave up, decreasing

$y = ax^{-b} \qquad a > 0, b > 0$

$y = ae^{-bx} \qquad a > 0, b > 0$

$y = a + bx + cx^2 \qquad b < 0, c < 0$

$y = A - \{\text{any from 2.}\}$

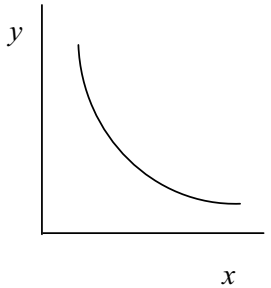

4. Concave down, decreasing

$y = a + bx + cx^2 \quad c < 0$

$y = A - \{\text{any from 1.}\}$

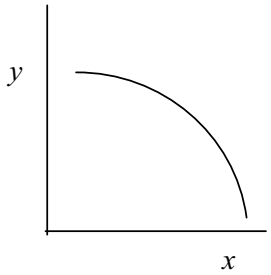

5. Sigmoid

$y = \dfrac{1}{a + be^{-cx}} \qquad a, b, c > 0$

$y = ax^b/(c + x^b) \quad a, c, > 0, b > 1$

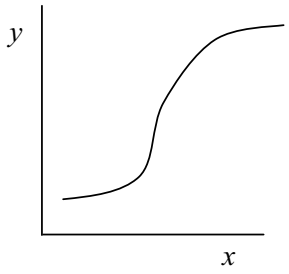

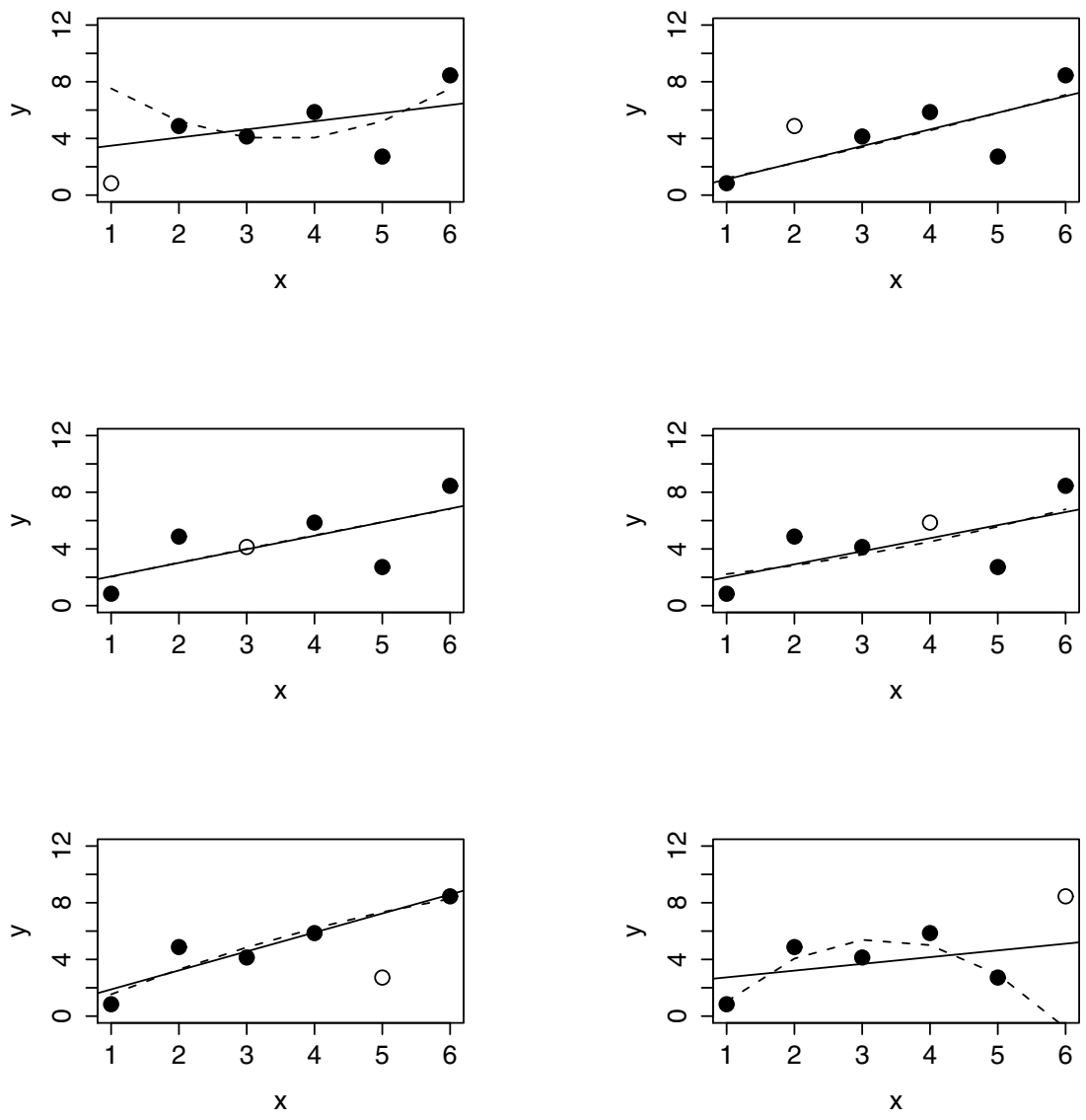

Figure 9.7: Cross validation for linear versus quadratic regression. In each panel, one of the 6 data points (shown as an open circle) is omitted from the data set, and the two models are fitted to the other data points. The solid line is the fitted linear model, the dashed line is the fitted quadratic.

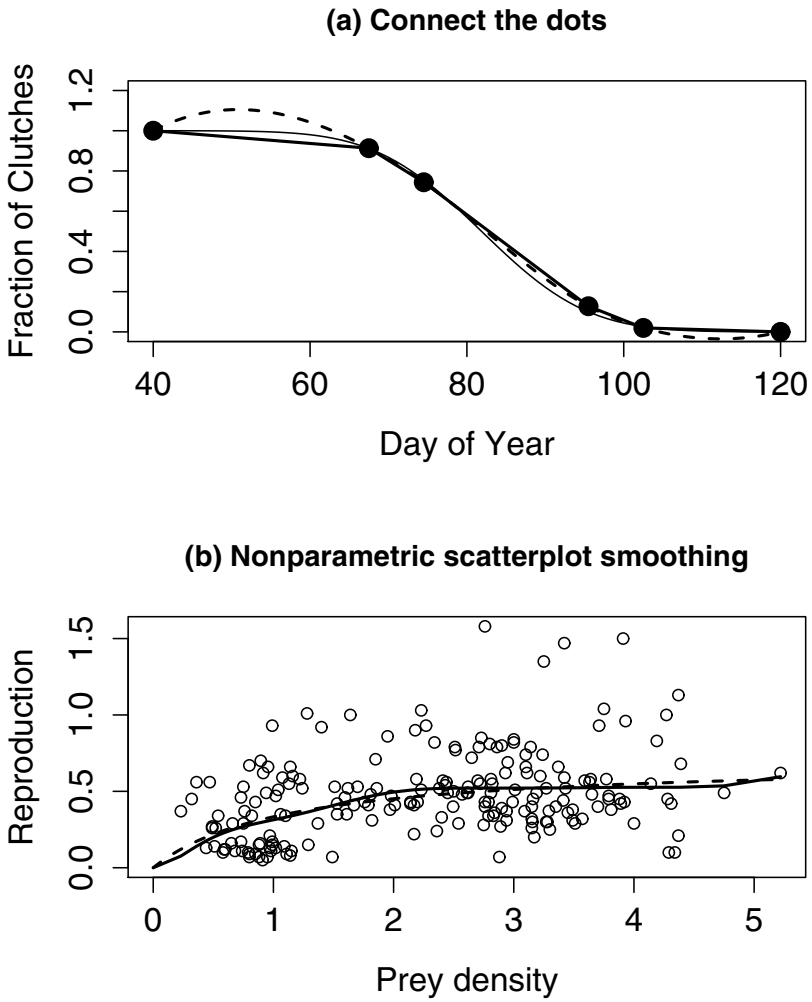

Figure 9.8: Examples of nonparametric rate equations based on data. (a) Two versions of "connect the dots". Heavy solid curve is linear interpolation, dashed curve is cubic spline interpolation. The light solid curve is a parametric model derived from population genetics theory for traits controlled by many genetic loci. (b) The solid curve is a nonparametric regression spline, fitted subject to the constraints of passing through $(0, 0)$ and being monotonically non-decreasing. For comparison, the dashed curve is the Michaelis-Menten model fitted to the same data ($\hat{V} = 0.7, \hat{K} = 1.1$)

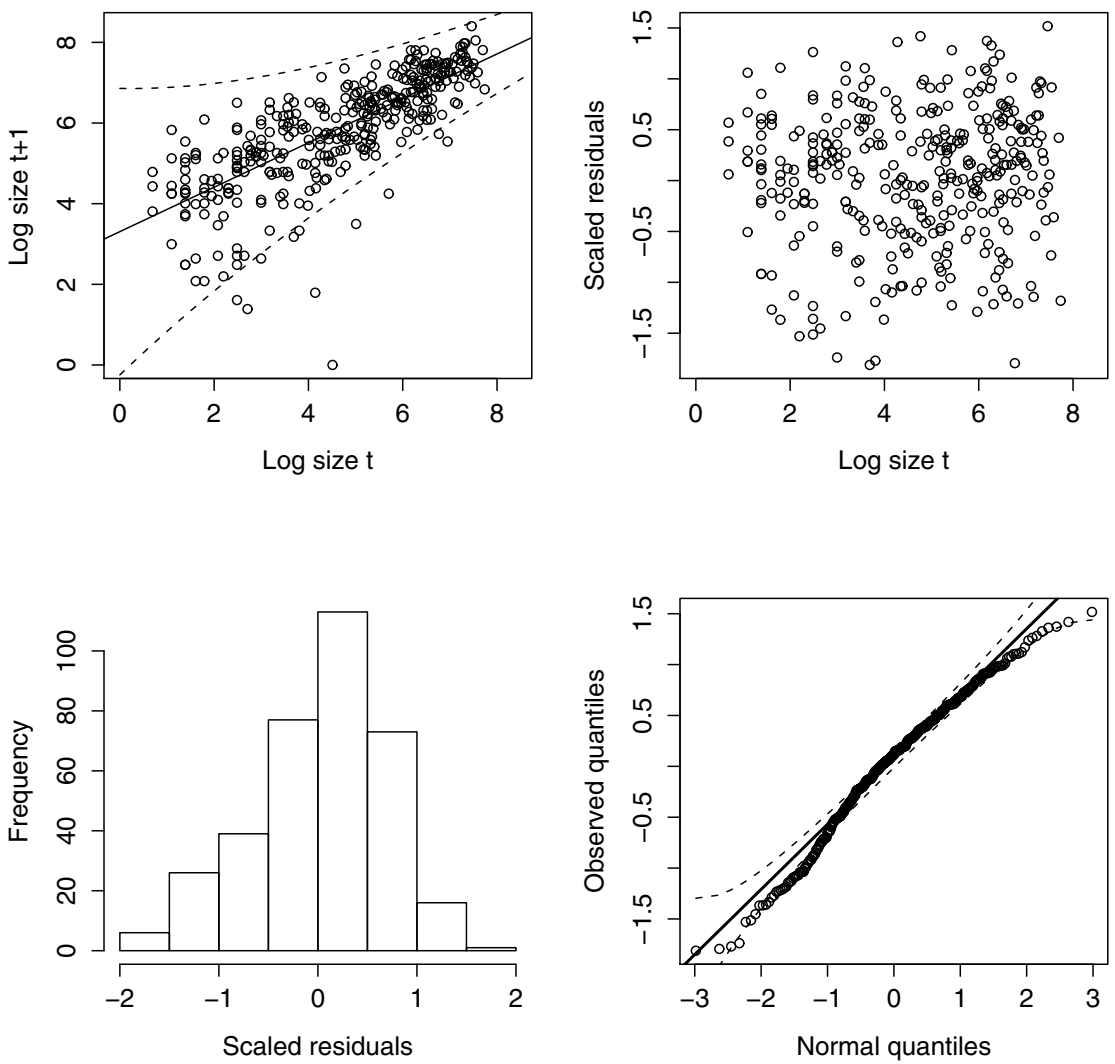

Figure 9.9: Fitting and testing a parametric model for the distribution of individual size in surviving plants of *Onopordum illyricum*, from Rees et al. 1999 (data provided by Mark Rees). Panels (clockwise from top left) show the data from one study site with fitted mean and variance functions, the scaled residuals versus original size, histogram and Normal quantile-quantile plot of scaled residuals.

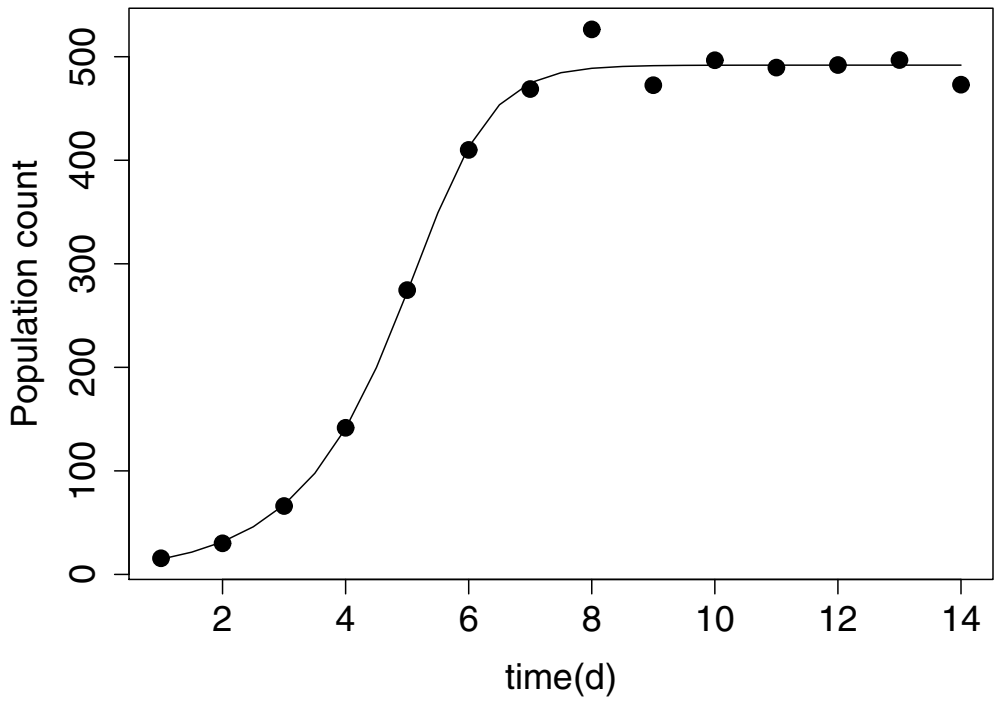

Figure 9.10: Results from calibration of the θ-logistic population model to data on population growth of *Paramecium aurelia* feeding on bacteria in Cerophyl growth medium; the data were digitized from Figure 2b in Veilleux (1976).

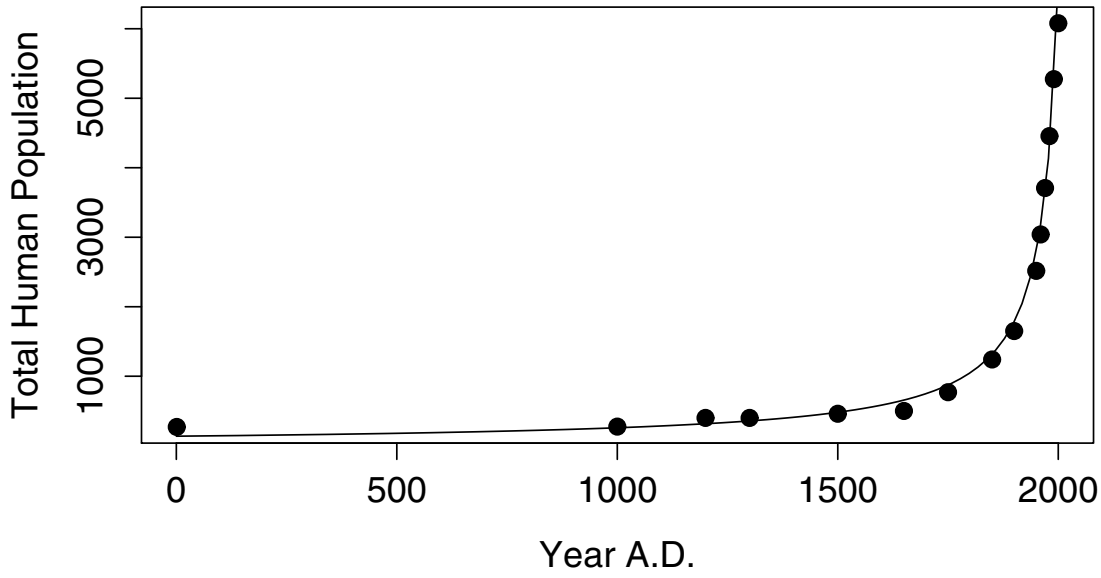

Figure 9.11: Solution of the Von Foerster et al. (1960) model (line) for the growth of total human population (solid dots, in millions), with parameters estimated by least squares on square-root scale. Population estimates were obtained from the International Programs Center of the US Census Bureau (online: www.census.gov/ipc/www), accessed June 16, 2003. For 1950 and earlier, the value used was the median of tabulated historical estimates; for subsequent dates the Census Bureau estimate was used.